Preprints.org

Article

Not peer-reviewed version

Cu^{2+} Intercalation and Structural Water Enhance Electrochemical Performance of Cathode in Zinc-Ion Batteries

He Lin *, Mengdong Wei , Yu Zhang

Posted Date: 8 July 2025

doi: 10.20944/preprints202507.0717.v1

Keywords: zinc-ion batteries; cathode materials; copper; structural water

Preprints.org is a free multidisciplinary platform providing preprint service that is dedicated to making early versions of research outputs permanently available and citable. Preprints posted at Preprints.org appear in Web of Science, Crossref, Google Scholar, Scilit, Europe PMC.

Copyright: This open access article is published under a Creative Commons CC BY 4.0 license, which permit the free download, distribution, and reuse, provided that the author and preprint are cited in any reuse.

Preprints.org (www.preprints.org) | NOT PEER-REVIEWED | Posted: 8 July 2025 doi:10.20944/preprints202507.0717.v1

Disclaimer/Publisher's Note: The statements, opinions, and data contained in all publications are solely those of the individual author(s) and contributor(s) and not of MDPI and/or the editor(s). MDPI and/or the editor(s) disclaim responsibility for any injury to people or property resulting from any ideas, methods, instructions, or products referred to in the content.

Article

Cu^{2+} Intercalation and Structural Water Enhance Electrochemical Performance of Cathode in Zinc-Ion Batteries

He Lin*, Mengdong Wei and Yu Zhang

State Key Laboratory of Chemistry and Utilization of Carbon Based Energy Resources, College of Chemistry, Xinjiang University, Urumqi, 830017, Xinjiang, China

* Correspondence: helin@xju.edu.cn; Tel.: +86-180-4090-9207

Abstract

This study investigates the performance of Cu-intercalated $V_3O_7{\cdot}H_2O$ (CuVOH) as a cathode material for aqueous zinc-ion batteries (AZIBs). DFT calculations were conducted to explore the effects of Cu^{2+} incorporation and structural water on the electrochemical performance of VOH. The results indicated that Cu^{2+} and structural water enhance Zn^{2+} diffusion by reducing electrostatic resistance and facilitating faster transport. Based on these insights, CuVOH nanobelts were synthesized via a one-step hydrothermal method. The experimental results confirmed the DFT predictions, demonstrating that CuVOH exhibited an initial discharge capacity of 336.1 mAh g^{-1} at 0.2 A g^{-1} and maintained a high cycling stability with 98.7% retention after 1000 cycles at 10 A g^{-1}. The incorporation of Cu^{2+} pillars and interlayer water improved the structural stability and Zn^{2+} diffusion, offering enhanced rate performance and long-term cycling stability. The study highlights the effective integration of computational and experimental methods to optimize cathode materials for high-performance AZIBs, providing a promising strategy for the development of stable and efficient energy storage systems.

Keywords: zinc-ion batteries; cathode materials; copper; structural water

1. Introduction

With the continuous depletion of non-renewable fossil fuels, the global energy shortage has become an increasingly urgent issue [1]. To address the energy scarcity and mitigate the environmental crises caused by conventional fossil fuels, there is an urgent need to develop and utilize renewable clean energy sources, such as wind, solar, and tidal energy, to meet the immense energy demand of human society [2,3]. However, these renewable energy sources are prone to environmental influences and suffer from intermittency and uncontrollability, which limit their stable utilization and significantly hinder large-scale development and practical applications [4]. Therefore, the development of efficient energy storage and conversion media, along with the establishment of suitable electrochemical energy storage systems, is essential to facilitate the effective utilization of renewable energy [5].

Among various energy storage technologies, lithium-ion batteries (LIBs) have been widely applied in mobile electronic devices, such as smartphones, and in the new energy electric vehicle industry due to their high energy density and high operating voltage [6–8]. These advances represent a significant breakthrough in current energy storage technology. However, LIBs face numerous challenges: on one hand, the limited abundance of lithium in the Earth's crust leads to relatively high costs; on the other hand, the high cost, environmental pollution, and flammability of organic electrolytes pose serious safety hazards during battery use [9]. These challenges greatly restrict the further development and application of LIBs, necessitating the exploration of alternative energy storage technologies that are more sustainable and safer.

© 2025 by the author(s). Distributed under a Creative Commons CC BY license.

Preprints.org (www.preprints.org) | NOT PEER-REVIEWED | Posted: 8 July 2025 doi:10.20944/preprints202507.0717.v1

From the perspective of long-term green and sustainable development, the need for the development of low-cost and high-safety new rechargeable secondary batteries has become evident. In recent years, rechargeable multivalent metal-ion batteries, such as Mg^{2+} [10], Zn^{2+} [11], Ca^{2+} [12], and Al^{3+} [13] batteries, have attracted considerable attention due to their significant cost advantages. These metals are abundant in the Earth's crust, effectively mitigating the risks associated with the shortage of lithium resources [14]. Furthermore, in multivalent metal-ion batteries, multi-electron transfer reactions enhance the theoretical capacity of these metal-ion batteries [15].

Among various multivalent metal-ion batteries, aqueous zinc-ion batteries (AZIBs) have drawn particular attention due to the unique characteristics of zinc as the negative electrode material. On one hand, zinc metal offers a high theoretical specific capacity of 820 mAh g^{-1}, while on the other hand, its moderate potential of −0.76 V (vs. SHE) provides a combination of low cost, high safety, and high-performance energy storage [16–20]. Additionally, compared to non-aqueous electrolytes, aqueous electrolytes have significantly higher ionic conductivity, reaching up to 1 S cm^{-1}, which contributes to the high-rate performance of the battery [21]. In terms of industrial production, AZIBs have an inherent advantage over LIBs that use expensive and flammable organic electrolytes. The manufacturing process of AZIBs does not require strict control of oxygen and moisture environments, thus simplifying the production process and reducing costs [22]. As a result, AZIBs show great potential for large-scale applications in electric vehicles and grid energy storage systems [23–26].

The cathode materials in AZIBs, as hosts for Zn^{2+} storage, directly control the working voltage, reversible capacity, and overall energy storage characteristics of the battery. Therefore, the development of high-performance cathode materials is crucial for improving the efficient energy storage and practical application of AZIBs. Current cathode materials that have been reported include vanadium-based compounds [27–30], manganese-based oxides and their derivatives [31], organic conjugated polymers [32], and Prussian blue analogs (PBAs) [33–36].

In recent years, vanadium-based compounds have garnered widespread interest for their high specific capacity, abundant resources, and notable economic advantages, making them the focus of extensive research in AZIBs. As a typical layered crystal structure, vanadium oxides offer efficient transport channels for Zn^{2+} insertion/extraction due to their unique layered framework and multi-valent characteristics, showcasing excellent electrochemical performance [37,38]. In earlier studies, various vanadium oxides, such as V_2O_5 [39], $V_5O_{12}{\cdot}6H_2O$ [40], VO_2 [41], V_6O_{13} [42], ZnV_2O_4 [43], and LiV_3O_8 [44], have been widely explored and applied as cathode materials in AZIBs. Among them, $V_3O_7{\cdot}H_2O$ (VOH) has gained significant attention due to its unique layered structure [45]. VOH consists of a V_3O_8 layered framework composed of VO_6 octahedra and VO_5 trigonal bipyramidal units, with adjacent layers connected by hydrogen bonds, offering good structural stability that facilitates the fast migration of Zn^{2+} ions. Additionally, the mixed valence states of V^{5+} and V^{4+} in VOH (with an average valence state of +4.67) provide rich redox active sites, further enhancing its theoretical capacity [46].

However, VOH materials still face several challenges in practical applications. Firstly, the strong electrostatic interaction between Zn^{2+} and the host framework increases the diffusion energy barrier of Zn^{2+} within the lattice, leading to slow Zn^{2+} insertion/extraction kinetics. Additionally, during the charge/discharge process, the crystal structure is prone to collapse due to the repeated insertion/extraction of Zn^{2+}, which leads to capacity degradation and poor cycling stability [47]. To address this issue, researchers have proposed a modification strategy involving the co-intercalation of cations and water molecules [48]. When the introduced metal has a higher electronegativity than the vanadium element in the host, the chemical bonds formed between the metal and the oxygen atoms in the framework effectively stabilize the layered structure and reduce structural stress during charge/discharge, thus minimizing volume expansion and structural collapse [49]. More importantly, the retained interlayer water molecules, in conjunction with the intercalated metal ions, work synergistically to maintain efficient Zn^{2+} transport channels, thereby achieving simultaneous optimization of structural stability and reaction kinetics.

© 2025 by the author(s). Distributed under a Creative Commons CC BY license.

Preprints.org (www.preprints.org) | NOT PEER-REVIEWED | Posted: 8 July 2025 doi:10.20944/preprints202507.0717.v1

Motivated by these challenges, we performed DFT calculations to investigate the effects of Cu^{2+} incorporation and the presence of structural water on the electronic structure and electrochemical performance of the VOH system. The results revealed that in the Cu-intercalated VOH (CuVOH), the electrostatic resistance to Zn^{2+} diffusion is significantly reduced. This enhancement is attributed to the synergistic effect of Cu^{2+} pillars and structural water, which together facilitate faster and more efficient Zn^{2+} transport.

Inspired by these theoretical insights, we successfully synthesized CuVOH nanobelt structures via a one-step hydrothermal method. Cu^{2+} acts as an interlayer pillar, stabilizing the framework through Cu-O bonds and expanding the interlayer spacing to 0.226 nm, providing a pathway for fast Zn^{2+} migration. Additionally, the presence of interlayer water molecules further enhances the Zn^{2+} transport dynamics. Electrochemical tests reveal that CuVOH exhibits an initial discharge specific capacity of 336.1 mAh g^{-1} at 0.2 A g^{-1} and maintains a discharge capacity of 169.5 mAh g^{-1} after 1000 cycles at a high current density of 10 A g^{-1}, with a capacity retention of 98.7%, demonstrating excellent cycling stability. The Cu^{2+} intercalation strategy significantly improves both the structural stability and the Zn^{2+} diffusion kinetics, enhancing the rate performance and cycling stability of the VOH cathode material. This study provides a new design approach for developing high-performance cathode materials for aqueous zinc-ion batteries.

2. Results and Discussion

2.1. DFT Calculations

We first conducted DFT calculations to explore the effects of Cu^{2+} incorporation and the presence of structural water on the electronic structure and electrochemical performance of the VOH system. The computational models consisted of the unmodified VOH layered structure (Figure 1a), CuVO with Cu^{2+} ions but without structural water (Figure 1b), and CuVOH with both Cu^{2+} ions and structural water (Figure 1c). The calculated Density of States (DOS) for these systems are presented in Figure 1d, revealing significant insights into the electronic properties of each configuration.

For the CuVO system without structural water, the results demonstrate a semi-metallic behavior, with a finite DOS at the Fermi level in the spin-up channel and semiconductor-like characteristics in the spin-down channel. This electronic structure suggests poor electrical conductivity, primarily due to the lack of substantial states available for conduction in the spin-down channel, which impedes efficient charge transport. The semi-metallic nature is a direct consequence of the Cu^{2+} ion introduction, which alters the local electronic structure but fails to enhance conduction sufficiently in the absence of structural water.

In contrast, the CuVOH system, which incorporates both Cu^{2+} ions and structural water, exhibits metallic behavior, as evidenced by the significantly broadened and enhanced DOS at the Fermi level for both spin-up and spin-down states. The presence of structural water serves as an electron donor, increasing the carrier concentration and optimizing the conduction pathways. This enhancement in electronic properties, attributed to the water's role in facilitating charge transport, leads to significantly improved conductivity compared to the CuVO system without structural water.

© 2025 by the author(s). Distributed under a Creative Commons CC BY license.

Preprints.org (www.preprints.org) | NOT PEER-REVIEWED | Posted: 8 July 2025 doi:10.20944/preprints202507.0717.v1

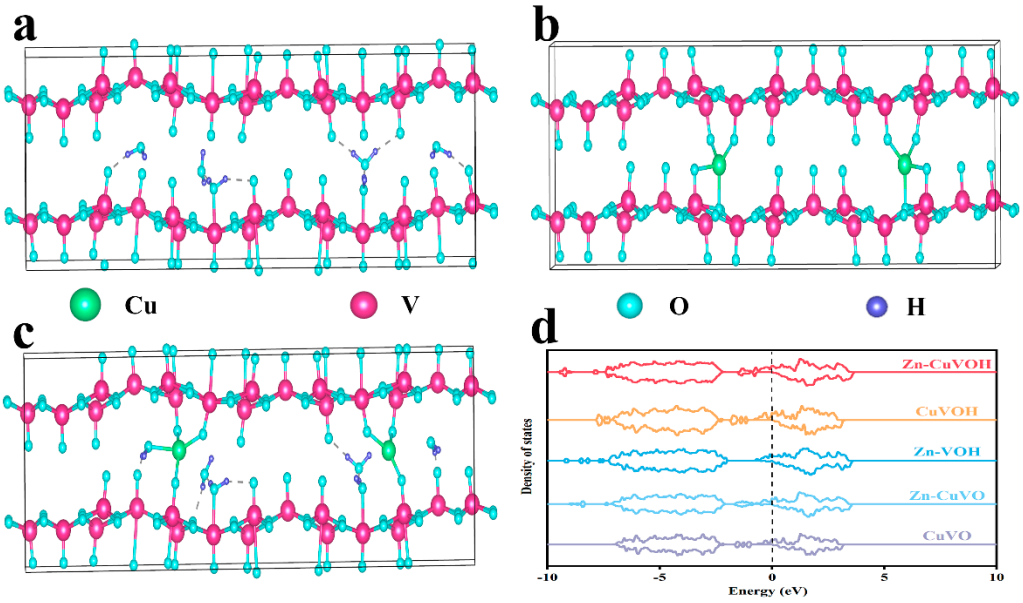

Figure 1. Structural configurations of (**a**) VOH, (**b**) CuVO and (**c**) CuVOH; (**d**) DOS of VOH, CuVO and CuVOH.

Moreover, the introduction of Zn^{2+} into the CuVOH system results in further improvements. The Zn-CuVOH system shows a substantial broadening and increased intensity of the DOS near the Fermi level, indicating a marked enhancement in the material's conductivity. This observation underscores the synergistic effect of Zn^{2+} incorporation, which effectively tunes the electronic structure to increase the overall carrier density. When compared to Zn-VOH, which lacks Cu^{2+} ions, the Zn-CuVOH system displays a significant increase in DOS near the Fermi level, suggesting that the CuVOH matrix provides a much more favorable electronic structure for enhanced charge transport.

In order to further elucidate the key effects of Cu^{2+} incorporation and structural water on the Zn^{2+} diffusion kinetics, we conducted a differential charge density analysis to reveal the charge transfer characteristics of different systems (Figure 2). The differential charge density maps highlight electron accumulation in yellow regions and electron depletion in blue regions, which provide crucial insights into the charge redistribution within each system. For the unmodified VOH system (Figure 2a), the differential charge density analysis indicates a significant charge rearrangement between the Zn atom and the host VOH material. The Zn atom loses a considerable amount of electrons (represented by the blue region), and these electrons predominantly transfer to the neighboring V and O atoms in the VOH structure (yellow regions). This substantial electron transfer suggests the presence of strong electrostatic interactions between Zn^{2+} and the VOH host, which are unfavorable for the efficient diffusion of Zn^{2+} ions.

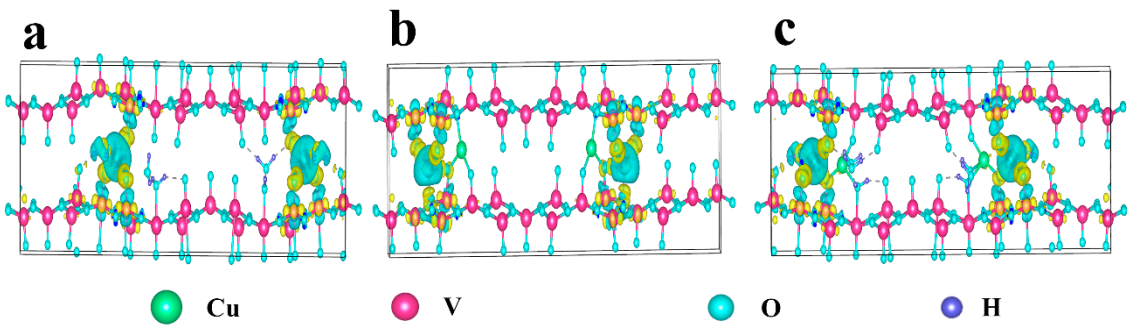

Figure 2. Differential charge density of (**a**) VOH, (**b**) CuVO and (**c**) CuVOH.

© 2025 by the author(s). Distributed under a Creative Commons CC BY license.

Preprints.org (www.preprints.org) | NOT PEER-REVIEWED | Posted: 8 July 2025 doi:10.20944/preprints202507.0717.v1

In the CuVO system, which does not contain structural water (Figure 2b), the electron transfer is primarily limited to interactions between Zn and the adjacent V and O atoms, with no significant electronic changes observed near the Cu atoms. This observation suggests that the Cu^{2+} ions do not directly participate in the charge compensation process and do not significantly influence the Zn^{2+} diffusion behavior. Consequently, the lack of participation of Cu^{2+} in the charge redistribution process further hinders the diffusion of Zn^{2+} in the CuVO system.

In contrast, the CuVOH system, which incorporates both Cu^{2+} ions and structural water (Figure 2c), exhibits a significantly different charge distribution. In this system, the electrons lost by Zn not only transfer to the neighboring V and O atoms but also partially transfer to the interlayer structural water molecules. This unique charge distribution indicates that the presence of structural water effectively screens the charge of the Zn^{2+} ions and establishes a smoother electrostatic environment in the interlayer. As a result, the electrostatic resistance to Zn^{2+} diffusion is substantially reduced, allowing for faster diffusion of Zn^{2+} ions within the CuVOH structure. This enhanced diffusion behavior is attributed to the cooperative effect of Cu^{2+} and the structural water molecules, which work synergistically to facilitate the efficient transport of Zn^{2+} ions. Overall, these findings suggest that CuVOH, owing to its unique electronic structure and the synergistic effect of Cu^{2+} and structural water, is a promising candidate for use in high-performance zinc-ion batteries.

2.2. Morphological Characterization

To verify the theoretical predictions from DFT calculations, the CuVOH material was synthesized via a one-step hydrothermal method. Quantitative elemental analysis was subsequently performed using Inductively Coupled Plasma Optical Emission Spectroscopy (ICP-OES), and the results are presented in Table 1. The ICP data indicate that the molar ratio of Cu to V in the CuVOH sample is approximately 1:17. This relatively low Cu content aligns well with the nominal stoichiometric ratio employed during synthesis, confirming the successful and controlled incorporation of Cu^{2+} ions into the VOH framework.

Table 1. ICP-OES results for the elemental composition of the synthesized CuVOH sample.

Element	Mass Content (mg kg^{-1})	Molar Amount (mmol kg^{-1})
Copper (Cu)	39,965	628.91
Vanadium (V)	567,432	11,138.89

The crystal structures of VOH and CuVOH were characterized by X-ray diffraction (XRD), as shown in Figure 3. The diffraction pattern of CuVOH closely matches that of the $V_3O_7{\cdot}H_2O$ phase (JCPDS No. 28-1433), indicating that the introduction of Cu^{2+} does not disrupt the original layered framework. Notably, a leftward shift of the (020) diffraction peak is observed in CuVOH compared to VOH, suggesting an expansion of the interlayer spacing. This shift is attributed to the incorporation of Cu^{2+} ions into the VOH lattice, which effectively enlarges the interlayer distance while preserving the structural integrity of the host material. The increased interlayer spacing is beneficial for zinc-ion storage, as it offers more accessible pathways for Zn^{2+} insertion and extraction, thereby improving the electrochemical kinetics and overall performance of the CuVOH cathode.

© 2025 by the author(s). Distributed under a Creative Commons CC BY license.

Preprints.org (www.preprints.org) | NOT PEER-REVIEWED | Posted: 8 July 2025 doi:10.20944/preprints202507.0717.v1

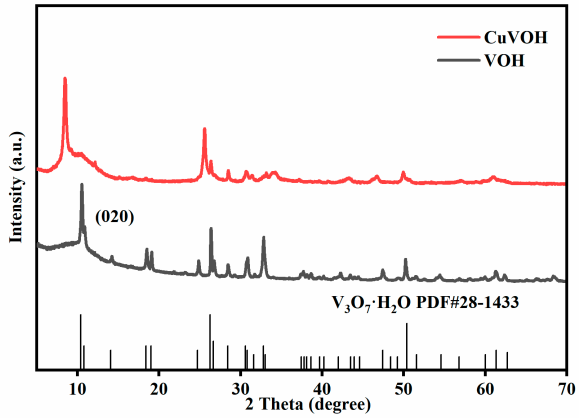

Figure 3. XRD patterns comparison of VOH and CuVOH samples.

To further investigate the molecular structure of the CuVOH material, Fourier Transform Infrared Spectroscopy (FT-IR) was conducted, and the resulting spectrum is presented in Figure 4a. The characteristic absorption bands observed at approximately 764 cm^{-1} and 1000 cm^{-1} are attributed to the stretching vibrations of V–O–V and terminal V=O bonds, respectively. These peaks are indicative of the preserved vanadium–oxygen framework, confirming the structural similarity between CuVOH and the parent VOH phase.

In addition, a distinct absorption peak at 1624 cm^{-1}, along with a broad band centered around 3400 cm^{-1}, can be ascribed to the bending vibration of H–O–H and the stretching vibration of O–H groups, respectively. These features provide strong evidence for the presence of interlayer or structural water molecules in the CuVOH material. The retention of these water-related vibrational features suggests that the incorporation of Cu^{2+} ions does not disrupt the hydration state of the host framework.

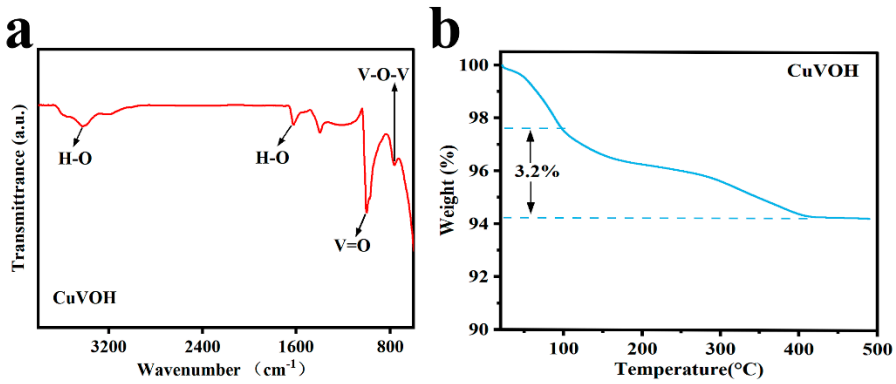

Figure 4. (**a**) FT-IR spectrum of CuVOH; (**b**) TGA curve of CuVOH.

To quantitatively assess the water content in the CuVOH material, thermogravimetric analysis (TGA) was conducted under a nitrogen atmosphere with a heating rate of 10 °C min^{-1} over the temperature range of 30–650 °C, as depicted in Figure 4b. The TGA curve exhibits a continuous weight loss upon heating, which stabilizes above approximately 400 °C, indicating the completion of the dehydration process.

The initial weight loss below 100 °C is attributed to the removal of physically adsorbed water on the surface of the CuVOH particles. The more substantial weight loss observed between 100 °C and 400 °C corresponds to the release of coordinated or interlayer structural water, which is integrated into the crystal lattice of CuVOH. The sharp mass decrease within this temperature window confirms the presence of chemically bound water molecules, which are essential for maintaining the layered configuration and facilitating ion transport.

© 2025 by the author(s). Distributed under a Creative Commons CC BY license.

Preprints.org (www.preprints.org) | NOT PEER-REVIEWED | Posted: 8 July 2025 doi:10.20944/preprints202507.0717.v1

Based on the total weight loss in the relevant temperature intervals and the quantitative elemental analysis from ICP-OES, the chemical composition of the synthesized CuVOH material can be deduced as $Cu_{0.17}V_3O_7 \cdot 0.5H_2O$.

To further verify the incorporation of Cu^{2+} and investigate the oxidation states of vanadium in the CuVOH material, X-ray photoelectron spectroscopy (XPS) analysis was performed (Figure 5a). The XPS spectra display distinct peaks corresponding to the binding energies of V, O, and Cu, confirming the successful incorporation of Cu^{2+} into the structure. The V 2p fine XPS spectrum, shown in Figure 5b, reveals peaks at binding energies of 517.4 eV and 516.1 eV, which are attributed to the presence of V^{5+} and V^{4+}, respectively. The incorporation of Cu^{2+} induces a slight reduction of V^{5+} to V^{4+}, leading to a mixed-valence state (V^{4+}/V^{5+}) that significantly enhances the material's electronic conductivity and electrochemical activity.

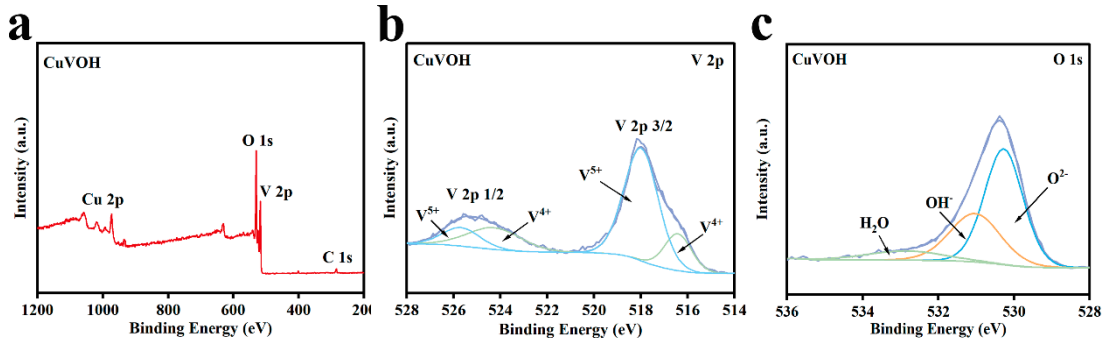

Figure 5. (**a**) XPS full spectrum of CuVOH; (**b**) V 2p fine spectrum of CuVOH; (**c**) O 1s fine spectrum of CuVOH.

Additionally, the O 1s spectrum in Figure 5c exhibits peaks at binding energies of 530.2 eV, 531.1 eV, and 532.6 eV, which are assigned to lattice oxygen (O^{2-}), surface-adsorbed oxygen (OH^-), and water molecules, respectively. These observations further confirm the presence of structural water in the CuVOH material, which aligns with the findings from FT-IR and TG analyses. The structural water provides a more favorable electrostatic environment for Zn^{2+} transport, thereby improving the electrochemical performance of the material.

Scanning electron microscopy (SEM) and transmission electron microscopy (TEM) were employed to investigate the morphological features of VOH and CuVOH materials. As shown in Figure 6a, the SEM image of VOH reveals a uniform and elongated nanobelt structure, with widths ranging from several hundred nanometers to a few micrometers. The TEM image (Figure 6b) further illustrates the characteristic nanobelt morphology of VOH, providing a clear visualization of the material's structure. Additionally, the high-resolution transmission electron microscopy (HRTEM) image (Figure 6c) reveals the crystalline structure of VOH, with a lattice spacing of 0.166 nm. This measurement corresponds to the (020) plane of the material, confirming the well-defined crystalline nature of the VOH structure. The elemental distribution map (Figure 6d) indicates a homogeneous distribution of V) and O elements along the nanobelts, suggesting the uniformity of the material's composition.

© 2025 by the author(s). Distributed under a Creative Commons CC BY license.

Preprints.org (www.preprints.org) | NOT PEER-REVIEWED | Posted: 8 July 2025 doi:10.20944/preprints202507.0717.v1

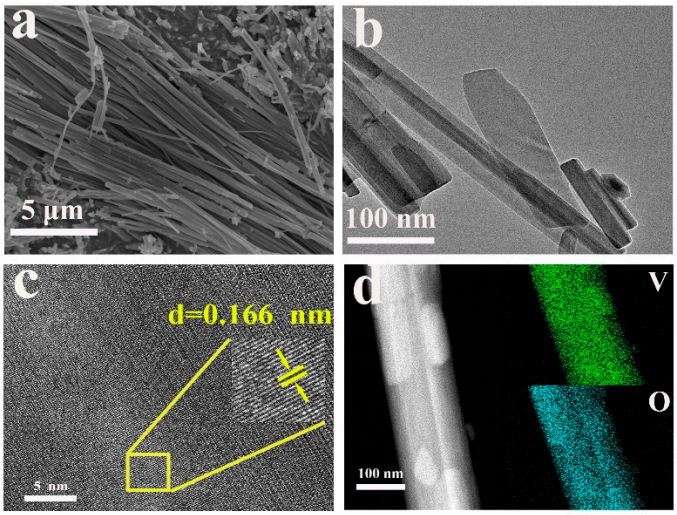

Figure 6. (**a**) SEM image of VOH; (**b**) TEM images of VOH; (**c**) HRTEM images of VOH and (**d**) corresponding elemental mapping.

Upon the incorporation of Cu^{2+}, significant changes in the morphology of the material were observed. SEM images of CuVOH (Figure 7a) show a uniform yet shorter nanobelt structure compared to VOH, which can be advantageous for enhancing electron transport rates and, consequently, the conductivity of the material. The HRTEM image (Figure 7b) further provides detailed insights into the microstructure of CuVOH, with a measured lattice spacing of 0.226 nm, corresponding to the (020) plane (Figure 7c). This increase in interlayer spacing is consistent with the leftward shift of the (020) diffraction peak observed in the XRD analysis, confirming that the embedding of Cu^{2+} ions effectively expands the interlayer spacing of the material. This expansion is crucial for improving the electrochemical performance of CuVOH, as it facilitates ion diffusion and enhances charge transport.

Furthermore, the elemental distribution map (Figure 7d) of CuVOH shows a uniform distribution of Cu, V, and O elements along the nanobelts, further corroborating the successful incorporation of Cu^{2+} ions and their even distribution within the material.

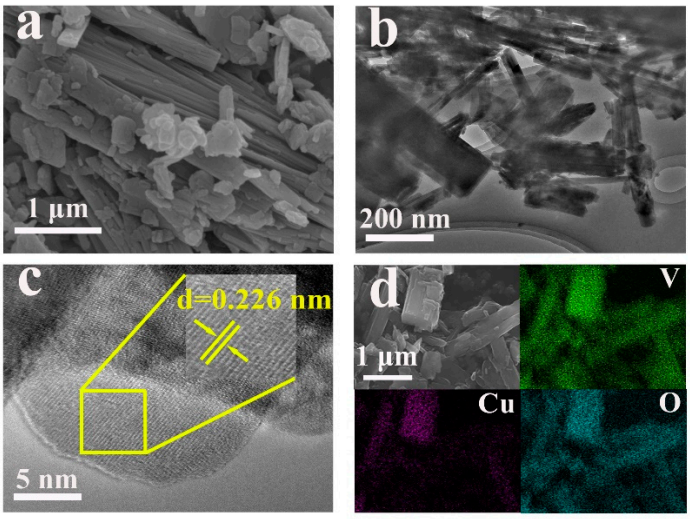

Figure 7. (**a**) SEM image of CuVOH; (**b**) TEM images of CuVOH; (**c**) HRTEM images of CuVOH and (**d**) corresponding elemental mapping.

© 2025 by the author(s). Distributed under a Creative Commons CC BY license.

Preprints.org (www.preprints.org) | NOT PEER-REVIEWED | Posted: 8 July 2025 doi:10.20944/preprints202507.0717.v1

2.3. Electrochemical Properties Characterization

To systematically evaluate the electrochemical performance of the VOH and CuVOH materials as cathodes, CR2032-type coin cells were assembled using each material as the active electrode. The cyclic voltammetry (CV) curves of the CuVOH electrode for the initial three cycles are shown in Figure 8a. Two pairs of well-defined redox peaks are observed at approximately 0.99/0.91 V and 0.58/0.48 V, which can be attributed to the V^{5+}/V^{4+} and V^{4+}/V^{3+} redox couples, respectively. These results confirm that the Zn^{2+} intercalation/deintercalation process in the CuVOH structure is accompanied by multiple-step redox reactions involving vanadium ions. Moreover, the nearly overlapping CV curves across the first three cycles indicate excellent electrochemical reversibility and high structural stability of the CuVOH electrode during repeated charge/discharge processes.

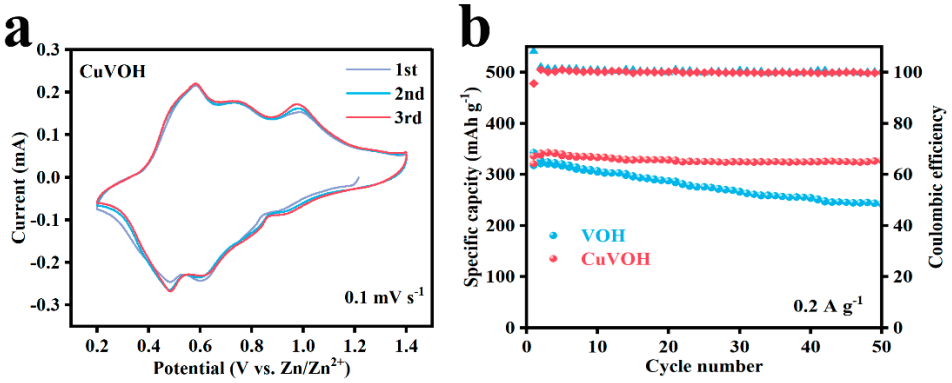

Figure 8. (**a**) CV curves for the first three turns of the CuVOH electrode at a scan rate of 0.1 mV s^{-1}; (b) Cycling performance plots of VOH and CuVOH electrodes at current density of 0.2 A g^{-1}.

The cycling performance of the VOH and CuVOH electrodes is compared in Figure 8b under a current density of 0.2 A g^{-1}. The VOH electrode shows a noticeable capacity fading behavior, with an initial discharge capacity of 317 mAh g^{-1} that gradually decreases to 241.6 mAh g^{-1} after 50 cycles, corresponding to a capacity retention of only 76.2%. In contrast, the CuVOH electrode delivers a higher initial discharge capacity of 336.1 mAh g^{-1} and maintains a remarkable capacity retention of 97.4% after 50 cycles. This significant enhancement in cycling performance can be attributed to the incorporation of Cu^{2+} ions, which improves the structural integrity and charge transport properties of the electrode material. These experimental observations are in good agreement with the theoretical predictions from DFT calculations, which suggested that the introduction of Cu^{2+} and structural water facilitates better Zn^{2+} diffusion and enhances the material's overall electrochemical stability. The superior electrochemical reversibility and long-term cycling stability of the CuVOH electrode underscore its great potential as a high-performance cathode material for AZIBs.

To further evaluate the cycling stability of the VOH and CuVOH electrodes, galvanostatic charge-discharge (GCD) measurements were conducted at a current density of 0.2 A g^{-1} over 50 cycles. As depicted in Figure 9a,b, the VOH electrode exhibits considerable variation in its charge-discharge profiles during cycling. This pronounced change in the voltage profile indicates inferior structural stability and a less reversible Zn^{2+} intercalation/deintercalation process. In contrast, the CuVOH electrode demonstrates highly overlapped GCD curves, with the 50th cycle remaining almost identical to the initial cycle. This excellent overlap provides compelling evidence of the enhanced structural stability and electrochemical reversibility of the CuVOH electrode.

© 2025 by the author(s). Distributed under a Creative Commons CC BY license.

Preprints.org (www.preprints.org) | NOT PEER-REVIEWED | Posted: 8 July 2025 doi:10.20944/preprints202507.0717.v1

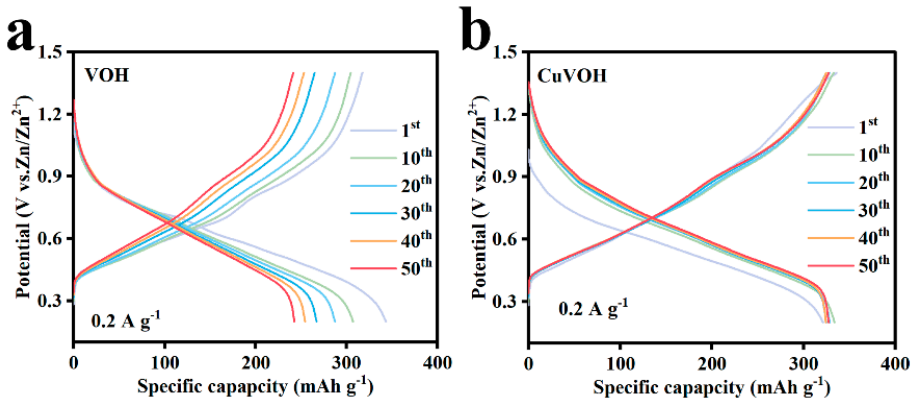

Figure 9. The galvanostatic charge-discharge curves of (**a**) VOH and (**b**) CuVOH for the first 50 cycles at a current density of 0.2 A g^{-1}.

To further evaluate the rate performance of the VOH and CuVOH cathode materials, their discharge capacities were systematically tested under various current densities, as shown in Figure 10a. The CuVOH electrode exhibited outstanding rate capability, delivering high specific discharge capacities of 369, 350, 309, 286, and 128 mAh g^{-1} at current densities of 0.1, 0.2, 1, 2, 5, and 10 A g^{-1}, respectively. Notably, when the current density was returned to 0.1 A g^{-1}, the discharge capacity recovered to 359 mAh g^{-1}, which is 97.3% of the initial capacity. This excellent capacity retention indicates superior structural stability and reversibility under high-rate conditions. In comparison, the VOH electrode showed significantly lower capacities under the same conditions, with discharge capacities of 306, 272, 224, 200, and 118 mAh g^{-1}, respectively, highlighting the performance enhancement induced by Cu^{2+} incorporation.

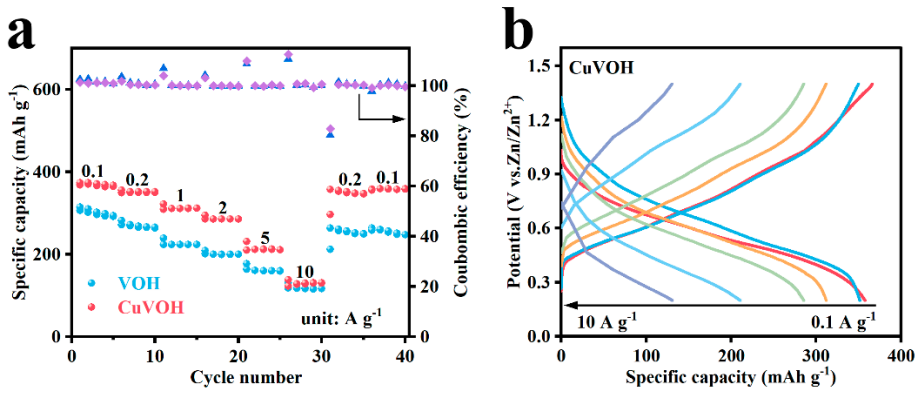

Figure 10. (**a**) Rate performance of VOH and CuVOH electrodes; (**b**) GCD curves of CuVOH at different current densities.

Figure 10b presents the GCD profiles of the CuVOH electrode at various current densities. As the current density increased, the charge-discharge curves maintained a consistent shape, albeit with slightly steeper slopes, indicating limited polarization and no obvious disappearance of plateaus. This observation suggests that CuVOH maintains efficient Zn^{2+} insertion/extraction kinetics and robust structural integrity even under high-rate operation.

The long-cycle stability of electrode materials is crucial for their practical applications in batteries, particularly when high current densities are involved. To further assess the structural stability and cycling durability of CuVOH electrodes under high current densities, long-cycle performance tests were conducted. As shown in Figure 11, the CuVOH electrode exhibited exceptional electrochemical performance. The material demonstrated an initial discharge capacity of 171.8 mAh g^{-1}, and after 1000 charge-discharge cycles, the specific capacity and capacity retention of CuVOH were 169.5 mAh g^{-1}

© 2025 by the author(s). Distributed under a Creative Commons CC BY license.

Preprints.org (www.preprints.org) | NOT PEER-REVIEWED | Posted: 8 July 2025 doi:10.20944/preprints202507.0717.v1

and 98.7%, respectively, with a near 100% Coulombic efficiency. This highlights its remarkable long-cycle stability.

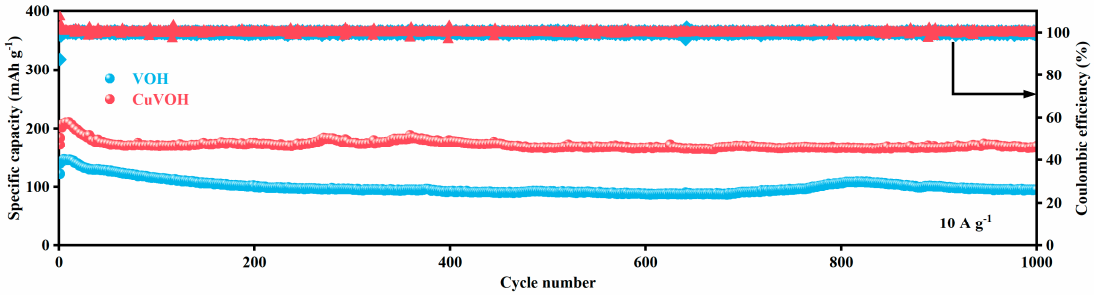

Figure 11. Long cycle performance of VOH and CuVOH electrodes at a current density of 10 A g^{-1}.

In contrast, the VOH electrode exhibited poor electrochemical stability under the same testing conditions. Its initial discharge capacity was 139.2 mAh g^{-1}, but after 1000 charge-discharge cycles, the discharge capacity decreased to 94.7 mAh g^{-1}, resulting in a capacity retention of only 68%. This significant deterioration further demonstrates that the unmodified VOH material suffers from poor cycling stability at high current densities.

The excellent long-cycle performance of the CuVOH can be primarily attributed to the incorporation of Cu^{2+} ions as "interlayer pillars" within the VOH structure. These Cu^{2+} ions form strong chemical bonds (Cu–O bonds) with the oxygen atoms, effectively stabilizing the layered structure and suppressing volume expansion and structural collapse during charge and discharge cycles. Furthermore, the presence of interlayer water molecules provides a smooth electrostatic environment for the rapid transport of Zn^{2+} ions, enhancing both the rate capability and cycling stability of the material.

The synergistic effect of Cu^{2+} ions and interlayer water significantly improves the long-cycle stability of CuVOH electrodes, especially under high current densities. This result further supports the findings from DFT calculations, which suggest that the structural modifications introduced by Cu^{2+} and interlayer water play a key role in enhancing the electrochemical performance of CuVOH.

To further investigate the role of structural water in determining the electrochemical performance of CuVOH, a comparative study was conducted using its dehydrated counterpart, CuVO. The XRD patterns of both samples are presented in Figure 12a. Notably, the (020) diffraction peak located at approximately 8.5° exhibited a significant reduction in intensity for CuVO compared to CuVOH. This weakening of the diffraction peak is attributed to the collapse of the layered structure during the dehydration process, which compromises the structural integrity of the material. The removal of interlayer water not only alters the crystal structure but also deteriorates the stability between adjacent layers, thereby reducing the robustness of the framework.

The adverse effect of dehydration on structural stability was further reflected in the cycling performance, as shown in Figure 12b,c. At a current density of 0.2 A g^{-1}, CuVOH demonstrated a high discharge capacity of 336.1 mAh g^{-1}, significantly outperforming CuVO, which delivered 284.7 mAh g^{-1}. More strikingly, under an ultra-high current density of 10 A g^{-1} after 1000 charge-discharge cycles, CuVOH still retained a reversible capacity of 169.5 mAh g^{-1}. In contrast, CuVO exhibited a much lower capacity of 108.5 mAh g^{-1} under the same conditions. These findings underscore the critical role of structural water in maintaining the layered framework and enhancing electrochemical properties. The presence of interlayer water serves as a structural stabilizer that mitigates collapse during Zn^{2+} insertion/extraction processes, while also possibly facilitating ion transport and charge transfer kinetics.

© 2025 by the author(s). Distributed under a Creative Commons CC BY license.

Preprints.org (www.preprints.org) | NOT PEER-REVIEWED | Posted: 8 July 2025 doi:10.20944/preprints202507.0717.v1

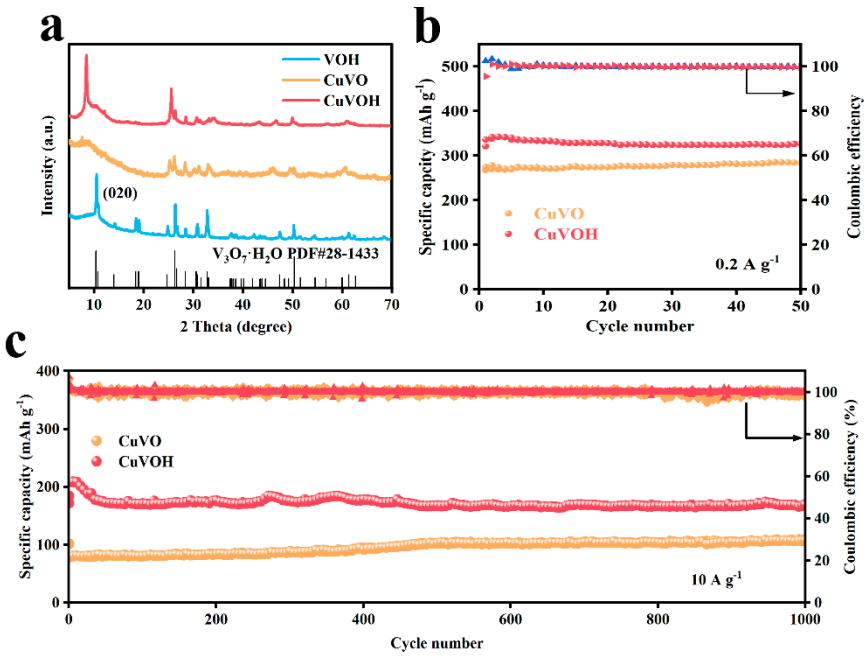

Figure 12. (a) XRD patterns of VOH, CuVO and CuVOH; (b) Cycling performance of CuVO and CuVOH at 0.2 A g^{-1}; (c) Long-term cycling performance of CuVO and CuVOH at 10 A g^{-1}.

To gain a deeper understanding of the charge storage mechanism of the CuVOH cathode material, CV measurements were conducted to investigate its redox behavior. As shown in Figure 13a,c, the CV curves of both VOH and CuVOH electrodes were recorded at various scan rates ranging from 0.1 to 1.0 mV s^{-1}. Both electrodes exhibit well-defined and reversible redox peaks, with minimal peak shifts observed as the scan rate increases, indicating good electrochemical reversibility.

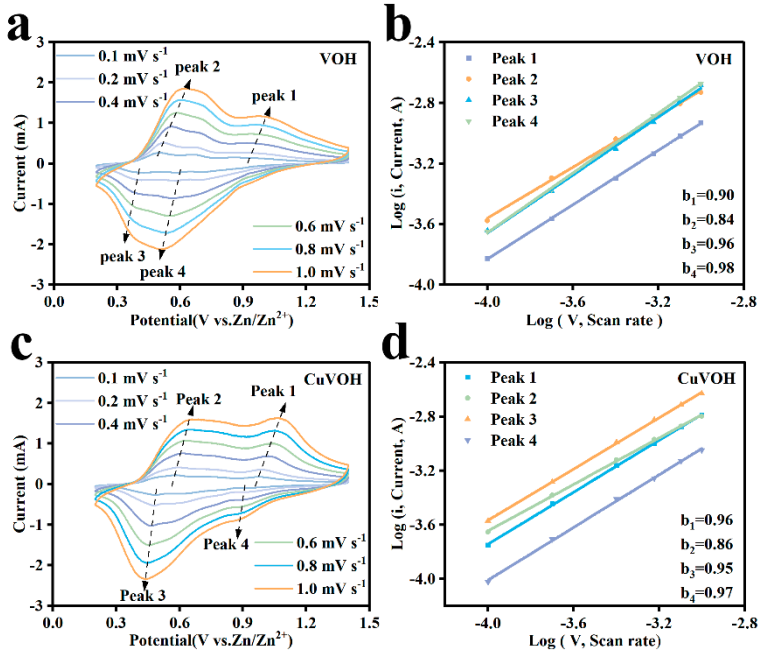

Figure 13. CV curves of (**a**) VOH and (**c**) CuVOH at various scan rates; Log (*i*) vs. log (*v*) plots of the four peaks in the CV curves for (**b**) VOH and (**d**) CuVOH.

© 2025 by the author(s). Distributed under a Creative Commons CC BY license.

Preprints.org (www.preprints.org) | NOT PEER-REVIEWED | Posted: 8 July 2025 doi:10.20944/preprints202507.0717.v1

To elucidate the kinetics of the electrochemical processes, the relationship between peak current (i) and scan rate (v) was analyzed according to the power-law equation:

$$i = av^b \quad (1)$$

Here, the b-value serves as a crucial indicator of the charge storage mechanism. A b-value close to 1.0 suggests a surface-controlled capacitive process, while a value near 0.5 indicates a diffusion-controlled behavior. The b-values were obtained by fitting the linear plots of log(i) versus log(v). As shown in Figure 13b, the b-values for the four redox peaks of the VOH electrode fall within the range of 0.5 to 1.0, suggesting a combination of surface capacitive effects and diffusion-controlled Faradaic reactions. In contrast, the CuVOH electrode (Figure 13d) exhibits b-values that are much closer to 1.0, indicating a dominant capacitive behavior.

Further quantitative differentiation between capacitive and diffusion-controlled contributions was carried out using the following equations:

$$i = k_1v + k_2v^{1/2} \quad (2)$$

Here, k_1v represents the contribution from capacitive processes (including electrical double-layer capacitance and surface redox pseudocapacitance), while $k_2v^{1/2}$ corresponds to the diffusion-limited Faradaic contribution. The total current can thus be deconvoluted to determine the relative contributions of each process.

Based on this analysis, the capacitive contribution ratios at various scan rates were calculated (Figure 14a,b). For the VOH electrode, the capacitive contribution increased from 71% at 0.1 mV s^{-1} to 88% at 1.0 mV s^{-1}. Notably, the CuVOH electrode demonstrated an even more pronounced capacitive dominance, with the contribution rising from 81% to 93% over the same range. This enhancement in capacitive behavior is primarily attributed to the incorporation of Cu^{2+}, which improves the intrinsic electrical conductivity of the material and facilitates faster surface reactions.

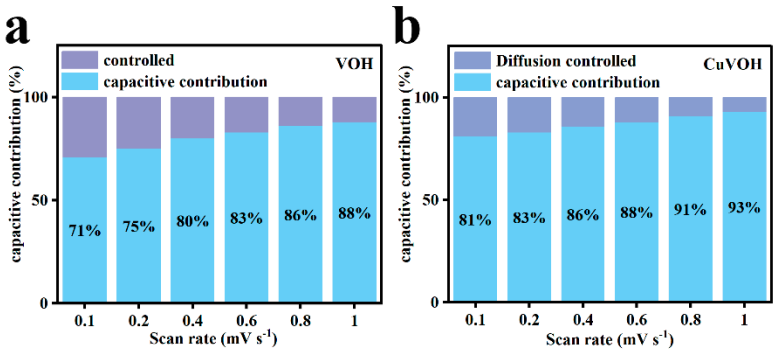

Figure 14. Capacitance contribution of (**a**) VOH and (**b**) CuVOH at different scan rates.

The high capacitive contribution observed in CuVOH is consistent with its previously demonstrated superior rate performance, as surface-controlled processes typically enable faster electrochemical responses. These results underscore the critical role of Cu^{2+} incorporation in modulating the charge storage kinetics and enhancing the high-rate capability of vanadium-based cathode materials for zinc-ion batteries.

To further elucidate the origin of the enhanced rate performance of the CuVOH cathode, galvanostatic intermittent titration technique (GITT) was employed to quantitatively evaluate the Zn^{2+} diffusion kinetics. As shown in Figure 15a, the Zn^{2+} diffusion coefficients for the pristine VOH electrode are in the range of 10^{-16} to 10^{-14} cm s^{-1}. In contrast, the CuVOH electrode (Figure 15b) exhibits a significantly higher diffusion coefficient ranging from 10^{-13} to 10^{-12} cm s^{-1}, which is approximately 2–3 orders of magnitude greater than that of VOH. This substantial enhancement in ion diffusion suggests that the intercalation of Cu^{2+} ions effectively optimizes the diffusion pathways for Zn^{2+} transport within the layered structure, thereby facilitating faster ionic movement. The higher

© 2025 by the author(s). Distributed under a Creative Commons CC BY license.

Preprints.org (www.preprints.org) | NOT PEER-REVIEWED | Posted: 8 July 2025 doi:10.20944/preprints202507.0717.v1

diffusion coefficients of CuVOH not only contribute to superior rate capability but also play a crucial role in suppressing undesirable side reactions during cycling. Efficient ion transport reduces the concentration polarization and ensures more uniform Zn^{2+} insertion/extraction, which in turn enhances the cycling stability of the electrode.

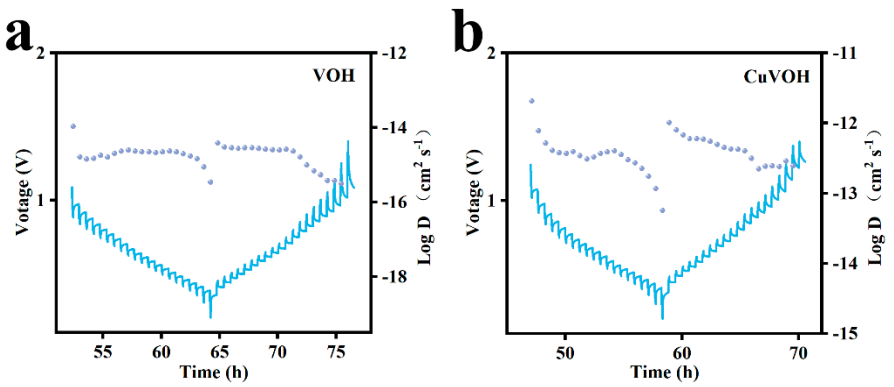

Figure 15. Capacitance contribution of (**a**) VOH and (**b**) CuVOH at different scan rates.

In addition, electrochemical impedance spectroscopy (EIS) was conducted before and after 50 charge/discharge cycles at a current density of 0.2 A g^{-1} to assess the interfacial charge transfer kinetics. As illustrated in Figure 16, the charge transfer resistance (R_{ct}) of the CuVOH electrode shows a noticeable decrease after cycling, indicating an activation process during the electrochemical reactions. This reduction in R_{ct} reflects the improved charge transport and interfacial reaction kinetics, further supporting the enhanced electrochemical reversibility and long-term cycling stability of the CuVOH electrode.

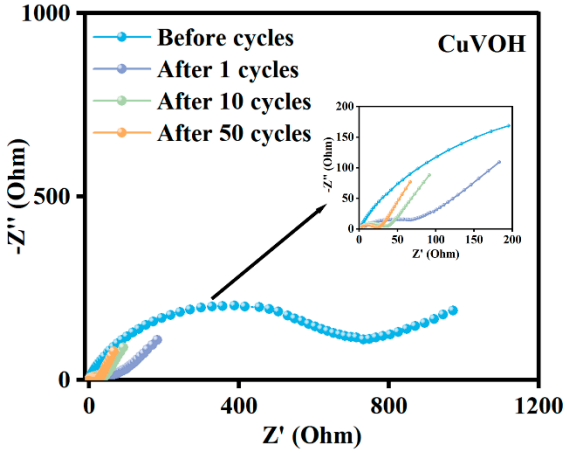

Figure 16. Nyquist plots of CuVOH electrode before and after cycling.

3. Materials and Methods

3.1. Calculation Method

DFT calculations were performed using the Vienna Ab initio Simulation Package (VASP) [50]. The exchange–correlation interactions were treated using the Perdew–Burke–Ernzerhof (PBE) functional within the generalized gradient approximation (GGA) [51]. The interactions between the core and valence electrons were described by the Projector Augmented Wave (PAW) method [52,53]. A plane-wave basis set with a kinetic energy cutoff of 400 eV was employed to ensure accurate representation of the electronic wavefunctions. The convergence criteria were set to a total energy

© 2025 by the author(s). Distributed under a Creative Commons CC BY license.

Preprints.org (www.preprints.org) | NOT PEER-REVIEWED | Posted: 8 July 2025 doi:10.20944/preprints202507.0717.v1

tolerance of 1×10^{-5} eV for the self-consistent field (SCF) calculations, and a maximum residual force threshold of 0.01 eV $Å^{-1}$ for structural relaxation. The Brillouin zone was sampled using a Γ-centered k-point mesh of 4 × 4 × 4 for both geometry optimization and total energy calculations.

3.2. Preparation of Material

In the synthesis of VOH, 3.6 mmol of V_2O_5 was initially dispersed in a mixture of 64 mL deionized water and 2 mL acetone. The solution was stirred continuously at room temperature for 4 hours to ensure complete dispersion of V_2O_5. The resulting mixture was then transferred to a high-pressure autoclave, which was sealed and placed in an oven for hydrothermal treatment at 180 °C for 36 hours. Upon completion of the reaction, the autoclave was allowed to cool naturally to room temperature. The product was then washed alternately with deionized water and anhydrous ethanol three times to remove any residual reactants and byproducts. Finally, the product was dried under vacuum at 50 °C for 12 hours to yield the VOH material.

For the synthesis of CuVOH, 3.6 mmol of V_2O_5 was first dispersed in a mixture of 64 mL deionized water and 2 mL acetone, and the solution was magnetically stirred at room temperature for 4 hours. Subsequently, 0.1872 g of $Cu(NO_3)_2{\cdot}3H_2O$ was added to the solution, and the mixture was stirred for an additional hour. The resulting solution was then transferred to a high-pressure autoclave and subjected to a hydrothermal reaction at 180°C for 36 hours. Upon completion of the reaction, the autoclave was allowed to cool naturally to room temperature. The solid product at the bottom of the autoclave was collected and washed alternately with anhydrous ethanol and deionized water to remove impurities. Finally, the washed product was dried under vacuum at 50 °C for 12 hours to obtain the CuVOH material.

3.3. Materials Characterization

Structural characterization of the synthesized cathode materials was conducted through XRD analysis using Cu Kα radiation on a Smart Lab SE system (Tokyo, Japan). This method provided detailed insights into the crystalline phases, structural integrity, and potential phase transitions of the materials. The XRD patterns were carefully analyzed to identify distinct peaks corresponding to various crystalline planes, which facilitated the evaluation of material purity and crystallinity.

Morphological characterization was performed using SEM and TEM. SEM images were captured with a Hitachi SU8220 system (Tokyo, Japan), offering high-resolution surface imaging to examine the topography and particle distribution of the materials. Additionally, TEM analysis was carried out using an FEI Talos F200X system (Waltham, MA, USA), providing high-magnification insights into the internal morphology and nanostructural features of the cathode materials, thereby enabling visualization of fine details at the atomic scale.

The elemental composition and distribution across the materials were further investigated using energy dispersive X-ray spectroscopy (EDS) integrated with the SEM system. This technique allowed for both quantitative and qualitative determination of the elemental composition at various locations within the samples, offering a comprehensive view of the uniformity and purity of the materials. To complement this analysis, inductively coupled plasma optical emission spectroscopy (ICP-OES) was employed with an Optima 8000 system (MA, USA) for precise, quantitative measurements of elemental content, including trace metals, in the cathode materials.

FT-IR spectroscopy was employed to identify the functional groups within the materials. FT-IR analyses were performed using a VERTEX 70 system (Saarbrücken, Germany), providing detailed spectra of molecular vibrations, which provided valuable information on the chemical bonds and functional groups present. This data was crucial for elucidating the chemical composition and bonding environment of the cathode materials. XPS was utilized to examine the surface chemistry and monitor the oxidation states of the elements in the materials. XPS measurements were conducted with a Thermo ESCALAB 250Xi system (Waltham, MA, USA).

3.4. Electrode Preparation and Battery Assembly

© 2025 by the author(s). Distributed under a Creative Commons CC BY license.

Preprints.org (www.preprints.org) | NOT PEER-REVIEWED | Posted: 8 July 2025 doi:10.20944/preprints202507.0717.v1

The electrode preparation process begins by mixing the active material, conductive agent (acetylene black), and binder (PVDF) in a mass ratio of 6:3:1. This mixture is then thoroughly ground for 30 minutes using an agate mortar to ensure uniformity. Subsequently, N-Methyl-2-pyrrolidone (NMP) solvent is slowly added to the mixture while stirring, resulting in a homogeneous slurry with an optimal viscosity. The slurry is then uniformly coated onto a 0.03 mm thick titanium foil current collector using the doctor blade coating method. The coating thickness is meticulously controlled to achieve an active material loading of 1–1.4 mg cm^{-2}. Following the coating, the electrode is dried in a vacuum oven at 80 °C for 12 hours to completely remove the solvent. The dried electrode is then punched into circular discs with a diameter of 10 mm using a tablet press, preparing it for battery assembly.

To assess the electrochemical performance of the prepared electrode material, CR2032 coin-type cells are assembled. A 0.1 mm thick zinc foil is used as the anode, and a glass fiber separator (Whatman GF/D) is employed to separate the anode and cathode. The electrolyte consists of a 3 M $Zn(CF_3SO_3)_2$ aqueous solution. The prepared electrode is utilized as the cathode, and the assembly of the coin cell is conducted in an ambient atmosphere. After assembly, the coin cell is sealed using a coin cell crimping machine under hydraulic pressure to ensure a secure, airtight seal.

3.5. Electrochemical Measurements

The electrochemical measurements were performed using a CHI 760E electrochemical workstation in a coin cell configuration with two electrodes. The cathode sheet, coated with the active material, was used as the working electrode. CV was carried out within a voltage range of 0.2 V to 1.6 V (vs. Zn/Zn^{2+}), employing varying scan rates of 0.1, 0.2, 0.4, 0.6, 0.8, and 1 mV s^{-1} to analyze the electrochemical behavior of the electrode. The CV tests provided valuable insights into the redox reactions occurring at the electrode surface, revealing the kinetics and charge transfer characteristics of the material.

The EIS was conducted to measure the impedance of the system using a small-amplitude sinusoidal AC signal. The frequency range was set from 0.01 Hz to 100 kHz, with a voltage amplitude of 5 mV. The obtained data were analyzed using equivalent circuit modeling to evaluate the internal resistance and charge transfer resistance of the electrodes. This approach provided important information on the electrochemical behavior of the materials, especially in terms of their performance under different charge/discharge conditions.

In addition, the GITT was employed to investigate the diffusion processes and the relationship between charge transfer and electrochemical reactions at the electrode surface. This technique involved cycles of pulse application, constant current, and relaxation, allowing for the determination of the chemical diffusion coefficient. The GITT analysis provided further understanding of the material's transport properties and its ability to facilitate ion diffusion during charge and discharge cycles.

Furthermore, electrochemical cycling and rate capability tests were performed on the coin cells at room temperature. These tests involved continuous cycling within a voltage range of 0.2 V to 1.6 V, utilizing the CT2001A Battery Test System from Wuhan LAND Electric Co. The cycling tests assessed the stability and capacity retention of the electrodes over multiple charge/discharge cycles, while the rate capability tests measured the electrodes' performance under varying current densities. Collectively, these electrochemical measurements provided a comprehensive evaluation of the performance, stability, and transport properties of the examined electrode materials.

4. Conclusions

In conclusion, this study presents a comprehensive investigation into the potential of CuVOH as a high-performance cathode material for AZIBs, leveraging both DFT calculations and experimental validation. The DFT results provided valuable insights into the electrochemical behavior of CuVOH, revealing that the incorporation of Cu^{2+} ions and the presence of interlayer water molecules synergistically enhance Zn^{2+} diffusion kinetics by reducing the electrostatic resistance

© 2025 by the author(s). Distributed under a Creative Commons CC BY license.

Preprints.org (www.preprints.org) | NOT PEER-REVIEWED | Posted: 8 July 2025 doi:10.20944/preprints202507.0717.v1

within the framework. This theoretical understanding guided the successful synthesis of CuVOH nano-belt structures using a one-step hydrothermal method. The experimental results confirmed the predictions from DFT calculations, demonstrating that Cu^{2+} acts as an effective interlayer pillar, expanding the interlayer spacing and stabilizing the structure, while the interlayer water molecules improve the Zn^{2+} transport dynamics.

Electrochemical tests revealed that CuVOH exhibited an impressive initial discharge capacity of 336.1 mAh g^{-1} at 0.2 A g^{-1}, and after 1000 cycles at 10 A g^{-1}, it maintained a high capacity of 169.5 mAh g^{-1} with a capacity retention of 98.7%. These results underscore the critical role of Cu^{2+} intercalation and structural water in enhancing both the rate performance and cycling stability of the VOH cathode material. The combined DFT-experimental approach not only validates the potential of CuVOH for high-performance AZIB applications but also highlights the synergistic effect of Cu^{2+} and interlayer water as a core innovation. This study offers new avenues for the design and optimization of advanced cathode materials in energy storage systems, contributing to the development of more efficient and sustainable batteries for large-scale applications.

Author Contributions: Conceptualization, H.L. and M.W.; methodology, H.L. and Y.Z.; software, Y.Z.; validation, H.L., M.W. and Y.Z.; formal analysis, H.L. and M.W.; investigation, H.L., M.W. and Y.Z.; resources, M.W.; data curation, Y.Z.; writing—original draft preparation, H.L.; writing—review and editing, H.L., M.W. and Y.Z.; visualization, M.W. and Y.Z.; supervision, H.L.; project administration, H.L.; funding acquisition, H.L. All authors have read and agreed to the published version of the manuscript.

Funding: This research was funded by the Natural Science Foundation of the Xinjiang Uyghur Autonomous Region and the National Natural Science Foundation of China, grant number 22065032. The APC was funded by Graduate Education and Teaching Research and Reform Project of Universities in Xinjiang Autonomous Region, grant number XJ2025GY06.

Data Availability Statement: The data presented in this study are available on request from the corresponding author.

Acknowledgments: The authors acknowledge the Shiyanjia Lab (www.shiyanjia.com accessed on 5 March 2025) for the TEM tests.

Conflicts of Interest: The authors declare no conflicts of interest.

References

1. Algarni, S.; Tirth, V.; Alqahtani, T.; Alshehery, S.; Kshirsagar, P. Contribution of renewable energy sources to the environmental impacts and economic benefits for sustainable development. *Sustain. Energy. Techn.* **2023**, *56*, 103098.
2. Jia, X.; Liu, C.; Neale, Z.G.; Yang, J.; Cao, G. Active materials for aqueous zinc ion batteries: synthesis, crystal structure, morphology, and electrochemistry. *Chem. Rev.* **2020**, *120*, 7795–7866.
3. Gao, Y.; Zhang, H.; Liu, X.H.; Yang, Z.; He, X.X.; Li, L.; Qiao, Y.; Chou, S.L. Low-cost polyanion-type sulfate cathode for sodium-ion battery. *Adv. Energy Mater.* **2021**, *11*, 2101751.
4. Zeng, Y.; Lai, Z.; Han, Y.; Zhang, H.; Xie, S.; Lu, X. Oxygen-vacancy and surface modulation of ultrathin nickel cobaltite nanosheets as a high-energy cathode for advanced Zn-ion batteries. *Adv. Mater.* **2018**, *30*, 1802396.
5. Fan, L.; Ru, Y.; Xue, H.; Pang, H.; Xu, Q. Vanadium-based materials as positive electrode for aqueous zinc-ion batteries. *Adv. Sustainable Syst.* **2020**, *4*, 2000178.
6. Xu, J.; Cai, X.; Cai, S.; Shao, Y.; Hu, C.; Lu, S.; Ding, S. High-energy lithium-ion batteries: recent progress and a promising future in applications. *Energy Environ. Mater.* **2023**, *6*, e12450.
7. Jin, Y.; Zhang, T.; Zhang, M. Advances in intelligent regeneration of cathode materials for sustainable lithium-ion batteries. *Adv. Energy Mater.* **2022**, *12*, 2201526.
8. Shadike, Z.; Tan, S.; Wang, Q.C.; Lin, R.; Hu, E.; Qu, D.; Yang, X.Q. Review on organosulfur materials for rechargeable lithium batteries. *Mater. Horiz.* **2021**, *8*, 471–500.
9. Guo, N.; Huo, W.; Dong, X.; Sun, Z.; Lu, Y.; Wu, X.; Dai, L.; Wang, L.; Lin, H.; Liu, H.; Liang, H.; He, Z.; Zhang, Q. A review on 3D zinc anodes for zinc ion batteries. *Small* **2022**, *6*, 2200597.

© 2025 by the author(s). Distributed under a Creative Commons CC BY license.

Preprints.org (www.preprints.org) | NOT PEER-REVIEWED | Posted: 8 July 2025 doi:10.20944/preprints202507.0717.v1

10. Sari, D.; Rutt, A.; Kim, J.; Chen, Q.; Hahn, N.T.; Kim, H.; Persson, K.A.; Ceder, G. Alkali-ion-assisted activation of ε-$VOPO_4$ as a cathode material for Mg-ion batteries. *Adv. Sci.* **2024**, *11*, 2307838.
11. Zhu, Y.; Liang, G.; Cui, X.; Liu, X.; Zhong, H.; Zhi, C.; Yang, Y. Engineering hosts for Zn anodes in aqueous Zn-ion batteries. *Energy Environ. Sci.* **2024**, *17*, 369–385.
12. Yi, Y.; Xing, Y.; Wang, H.; Zeng, Z.; Sun, Z.; Li, R.; Lin, H.; Ma, Y.; Pu, X.; Li, M.M.J.; Park, K.Y.; Xu, Z.L. Deciphering anion-modulated solvation structure for calcium intercalation into graphite for Ca-ion batteries. *Angew. Chem. Int. Edit.* **2024**, *63*, e202317177.
13. Lu, C.; Zhao, F.; Tao, B.; Wang, Z.; Wang, Y.; Sheng, J.; Tang, G.; Wang, Y.; Guo, X.; Li, J.; Wei, L. Anode-free aqueous aluminum ion batteries. *Small* **2024**, *20*, 2402025.
14. Tan, Z.L.; Wei, J.X.; Liu, Y.; Zaman, F.; Rehman, W.; Hou, L.R.; Yuan, C.Z. V_2CT_x MXene and its derivatives: synthesis and recent progress in electrochemical energy storage applications. *Rare Met.* **2022**, *41*, 775–797.
15. Chen, R.; Luo, R.; Huang, Y.; Wu, F.; Li, L. Advanced high energy density secondary batteries with multi-electron reaction materials. *Adv. Sci.* **2016**, *3*, 1600051.
16. Zhong, M.; Wang, Y.; Xie, Y.; Yuan, S.; Ding, K.; Begin, E.J.; Zhang, Y.; Bao, J.L.; Wang, Y. Zinc-coordinated imidazole-based ionic liquid as liquid salt for all-temperature aqueous zinc-ion batteries. *Adv. Funct. Mater.* **2024**, *34*, 2316788.
17. Xiao, Y.; Ren, J.; Li, M.; Xiao, K.; Wang, Y. Charge-tuning mediated rapid kinetics of zinc ions in aqueous Zn-ion battery. *Chem. Eng. J.* **2023**, *474*, 145801.
18. Zhang, Y.; Liu, Z.; Li, X.; Fan, L.; Shuai, Y.; Zhang, N. Loosening zinc ions from separator boosts stable Zn plating/striping behavior for aqueous zinc ion batteries. *Adv. Energy Mater.* **2023**, *13*, 2302126.
19. Zhao, R.; Yang, J.; Han, X.; Wang, Y.; Ni, Q.; Hu, Z.; Wu, C.; Bai, Y. Stabilizing Zn metal anodes via cation/anion regulation toward high energy density Zn-ion batteries. *Adv. Energy Mater.* **2023**, *13*, 2203542.
20. Lee, Y.H.; Jeoun, Y.; Kim, J.H.; Shim, J.; Ahn, K.S.; Yu, S.H.; Sung, Y.E. Selective ion transport layer for stable aqueous zinc-ion batteries. *Adv. Funct. Mater.* **2024**, *34*, 2310884.
21. Wang, M.; Meng, Y.; Li, X.; Qi, J.; Li, A.; Huang, S. Challenges and strategies for zinc anodes in aqueous Zinc-ion batteries. *Chem. Eng. J.* **2025**, *507*, 160615.
22. Ma, L.; Liu, X.; Fan, J.; Yu, X.; Cao, L.; Zhao, C. Mass production of robust hydrogel electrolytes for high-performance zinc-ion batteries. *Mater. Horiz.* **2025**, *12*, 2736–2744.
23. Gao, Y.; Yin, J.; Xu, X.; Cheng, Y. Pseudocapacitive storage in cathode materials of aqueous zinc ion batteries toward high power and energy density. *J. Mater. Chem. A* **2022**, *10*, 9773–9787.
24. Li, L.; Jia, S.; Yue, S.; Wang, C.; Qiu, H.; Ji, Y.; Cao, M.; Zhang, D. Hydrogel-stabilized zinc ion batteries: progress and outlook. *Green Chem.* **2024**, *26*, 6404–6422.
25. Lee, D.; Kim, H.I.; Kim, W.Y.; Cho, S.K.; Baek, K.; Jeong, K.; Ahn, D.B.; Park, S.; Kang, S.J.; Lee, S.Y. Water-repellent ionic liquid skinny gels customized for aqueous Zn-ion battery anodes. *Adv. Funct. Mater.* **2021**, *31*, 2103850.
26. Pang, X.; An, B.; Zheng, S.; Wang, B. Cathode materials of metal-ion batteries for low-temperature applications. *J. Alloys Compd.* **2022**, *912*, 165142.
27. Lv, T.; Peng, Y.; Zhang, G.; Liang, S.; Yang, Z.; Yang, S.; Pang, H. How about vanadium-based compounds as cathode materials for aqueous zinc ion batteries? *Adv. Sci.* **2023**, *10*, 2206907.
28. Hu, H.; Zhao, P.; Li, X.; Liu, J.; Liu, H.; Sun, B.; Pan, K.; Song, K.; Cheng, H. Heterojunction tunnelled vanadium-based cathode materials for high-performance aqueous zinc ion batteries. *J. Colloid Interface Sci.* **2024**, *665*, 564–572.
29. Zhu, Y.; Dong, Y.; Li, J.; Li, Y.; Fan, Q.; Kuang, Q.; Zhao, Y. In situ electrochemical activation strategy toward organic cation preintercalated layered vanadium-based oxide cathode for high-performance aqueous zinc-ion batteries. *ACS Appl. Mater. Interfaces* **2025**, *17*, 16791–16801.
30. Chen, X.; Zhang, H.; Liu, J.-H.; Gao, Y.; Cao, X.; Zhan, C.; Wang, Y.; Wang, S.; Chou, S.-L.; Dou, S.-X.; Cao, D. Vanadium-based cathodes for aqueous zinc-ion batteries: mechanism, design strategies and challenges. *Energy Storage Mater.* **2022**, *50*, 21–46.
31. Liu, Y.; Wu, X. Strategies for constructing manganese-based oxide electrode materials for aqueous rechargeable zinc-ion batteries. *Chin. Chem. Lett.* **2022**, *33*, 1236–1244.

© 2025 by the author(s). Distributed under a Creative Commons CC BY license.

Preprints.org (www.preprints.org) | NOT PEER-REVIEWED | Posted: 8 July 2025 doi:10.20944/preprints202507.0717.v1

32. Sun, Q.Q.; Du, J.Y.; Sun, T.; Zhuang, Z.B.; Xie, Z.L.; Xie, H.M.; Huang, G.; Zhang, X.B. Spatial structure design of thioether-linked naphthoquinone cathodes for high-performance aqueous zinc–organic batteries. *Adv. Mater.* **2024**, *36*, 2313388.
33. Tan, Y.; Chen, Z.; Tao, Z.; Wang, A.; Lai, S.; Ho, S.; Yang, Y. Anion electrostatic insertion boosts efficient zinc ferrocyanide cathode for aqueous dual-ion battery. *Energy Storage Mater.* **2024**, *67*, 103274.
34. Beitia, J.; Ahedo, I.; Paredes, J.I.; Goikolea, E.; Larramendi, I.R. Exploring zinc-doped manganese hexacyanoferrate as cathode for aqueous zinc-ion batteries. *Nanomaterials* **2024**, *14*, 1092.
35. Ruo, H.; Chen, L.; Huang, J.; Lv, C.; Bai, J.; Xu, S.; Chen, J.; Zhang, D.; Yang, H. Constructing low-cost stable zinc-ion batteries with sodium-rich monoclinic manganese hexacyanoferrate cathode. *Surf. Interfaces* **2024**, *51*, 104594.
36. Zhang, M.; Zhao, W.; Yang, T.; Gao, R.; Luo, D.; Park, H.W.; Hu, Y.; Yu, A. Vacancy and growth modulation of cobalt hexacyanoferrate by porous MXene for zinc ion batteries. *Adv. Energy Mater.* **2024**, *14*, 2400543.
37. Tao, Y.; Zhang, H.J.; Luo, H.; Xue, Y. Advances of vanadium-based cathodes for aqueous zinc ion batteries. *Chem. Eur. J.* **2025**, *31*, e202500219.
38. Ding, J.; Gao, H.; Ji, D.; Zhao, K.; Wang, S.; Cheng, F. Vanadium-based cathodes for aqueous zinc-ion batteries: from crystal structures, diffusion channels to storage mechanisms. *J. Mater. Chem. A* **2021**, *9*, 5258–5275.
39. Zhu, Y.; Liu, X.; Hu, X.; Wang, T.; Parkin, I.P.; Wang, M.; Boruah, B.D. Polyaniline and water pre-intercalated V_2O_5 cathodes for high-performance planar zinc-ion micro-batteries. *Chem. Eng. J.* **2024**, *487*, 150384.
40. Xu, Q.; Chu, N.; Wang, Y.; Wang, H.; Xu, T.; Li, X.; Huang, S.; Li, X.; Luo, Y.; Yang, H.Y.; Kong, D. 3D printed low-tortuosity and ultra-thick hierarchical porous electrodes for high-performance wearable quasi-solid-state Zn-VOH batteries. *Adv. Sci.* **2025**, *12*, 2401660.
41. Wang, Z.; Cui, P.; Wang, X.; Chang, M.; Yu, Y.; You, J.; Hu, F.; Wu, Y.; Zhu, K. Co-substitution engineering boosting the kinetics and stablity of VO_2 for Zn ion batteries. *Adv. Funct. Mater.* **2024**, *34*, 2407925.
42. Wu, Z.; Yao, J.; Chen, C.; Chen, X.; Pan, X.; Zheng, J.; Gan, Y.; Li, J.; Liu, X.; Xia, C.; Lv, L.; Wang, H.; Wan, H. Ammonium intercalation engineering regulated structural stability of V_6O_{13} cathodes for durable zinc ion batteries. *Chem. Eng. J.* **2024**, *479*, 147889.
43. Jiang, H.; Yue, P.; Gao, Q.; Zhang, S.; Gao, M.; Wang, J.; Liu, Y.; Hou, L.; Chen, M., Yuan, C. Construction of nano ZnV_2O_4/N-doped porous carbon composites with optimized ionic and electronic conductivities as competitive cathodes toward zinc-ion capacitors. *Nanomaterials* **2024**, *10*, e202400445.
44. Wu, M.; Shi, C.; Yang, J.; Zong, Y.; Chen, Y.; Ren, Z.; Zhao, Y.; Li, Z.; Zhang, W.; Wang, L.; Huang, X.; Wen, W.; Li, X.; Ning, X.; Ren, X.; Zhu, D. The LiV_3O_8 superlattice cathode with optimized zinc ion insertion chemistry for high mass-loading aqueous zinc-ion batteries. *Adv. Mater.* **2024**, *36*, 2310434.
45. Pang, Q.; Sun, C.; Yu, Y.; Zhao, K.; Zhang, Z.; Voyles, P.M.; Chen, G.; Wei, Y.; Wang, X. $H_2V_3O_8$ nanowire/graphene electrodes for aqueous rechargeable zinc ion batteries with high rate capability and large capacity. *Adv. Energy Mater.* **2018**, *8*, 1800144.
46. Kuhn, A.; Pérez-Flores, J.C.; Prado-Gonjal, J.; Morán, E.; Hoelzel, M.; Díez-Gómez, V.; Sobrados, I.; Sanz, J.; García-Alvarado, F. Lithium intercalation mechanism and critical role of structural water in layered $H_2V_3O_8$ high-capacity cathode material for lithium-ion batteries. *Chem. Mater.* **2022**, *34*, 694–705.
47. Chen, X.; Zhang, H.; Liu, J.H.; Gao, Y.; Cao, X.; Zhan, C.; Wang, Y.; Wang, S.; Chou, S.L.; Dou, S.X.; Cao, D. Vanadium-based cathodes for aqueous zinc-ion batteries: mechanism, design strategies and challenges. *Energy Storage Mater.* **2022**, *50*, 21–46.
48. Lv, T.; Zhu, G.; Dong, S.; Kong, Q.; Peng, Y.; Jiang, S.; Zhang, G.; Yang, Z.; Yang, S.; Dong, X.; Pang, H.; Zhang, Y. Co-intercalation of dual charge carriers in metal-ion-confining layered vanadium oxide nanobelts for aqueous zinc-ion batteries. *Angew. Chem. Int. Edit.* **2023**, *62*, e202216089.
49. Zhu, K.; Wu, T.; Huang, K. A high-voltage activated high-performance cathode for aqueous Zn-ion batteries. *Energy Storage Mater.* **2021**, *38*, 473–481.
50. Kresse, G.; Furthmüller, J. Efficient iterative schemes for ab initio total-energy calculations using a plane-wave basis set. *Phys. Rev. B* **1996**, *54*, 11169–11186.

© 2025 by the author(s). Distributed under a Creative Commons CC BY license.

Preprints.org (www.preprints.org) | NOT PEER-REVIEWED | Posted: 8 July 2025 doi:10.20944/preprints202507.0717.v1

51. Perdew, J.P.; Burke, K.; Ernzerhof, M. Generalized gradient approximation made simple. *Phys. Rev. Lett.* **1996**, *77*, 3865–3868.
52. Kresse, G.; Joubert, D. From ultrasoft pseudopotentials to the projector augmented-wave method. *Phys. Rev. B* **1999**, *59*, 1758–1775.
53. Blöchl, P.E. Projector augmented-wave method. *Phys. Rev. B* **1994**, *50*, 17953–17979.

Disclaimer/Publisher's Note: The statements, opinions and data contained in all publications are solely those of the individual author(s) and contributor(s) and not of MDPI and/or the editor(s). MDPI and/or the editor(s) disclaim responsibility for any injury to people or property resulting from any ideas, methods, instructions or products referred to in the content.

© 2025 by the author(s). Distributed under a Creative Commons CC BY license.